A local radial basis function collocation method for band structure computation of 3D phononic crystals

Zheng, H., Zhang, C. & Yang, J.

Original citation & hyperlink:
Zheng, H, Zhang, C & Yang, J 2020, 'A local radial basis function collocation method for band structure computation of 3D phononic crystals', Applied Mathematical Modelling, vol. 77, pp. 1954-1964.
https://dx.doi.org/10.1016/j.apm.2019.09.006

DOI 10.1016/j.apm.2019.09.006
ISSN 0307-904X

Publisher: Elsevier

A local radial basis function collocation method for band structure computation of 3D phononic crystals

H. Zheng[1], Ch Zhang[2], Z. Yang[3*]

[1] School of Civil Engineering and Architecture, Nanchang University, 330031, China

[2] Department of Civil Engineering, University of Siegen, D-57068 Siegen, Germany

[3] Centre for Built and Natural Environment, Coventry University, CV1 5FB, United Kingdom

Abstract: In this paper, we further extend the local radial basis function collocation method (LRBFCM) for efficient computation of band structures of phononic crystals from 2D to 3D. The proposed LRBFCM uses one fictitious node to tackle instability problems caused by calculation of derivatives of the wave pressure. A few examples of sound pressure wave propagation are modelled to validate the developed method. Comparisons with finite element modelling demonstrate the high stability and efficiency of the new method in computation of band structures of 3D phononic crystals.

Keywords: Phononic crystals, interface conditions, wave propagation, band structures, eigenvalue problems, radial basis functions.

1. Introduction

Due to periodic variations in material properties in periodic structures or metamaterials, acoustic, optical or elastic stress waves of a certain range of frequencies (between the bandgaps) cannot propagate [1, 2]. This phenomenon can be utilized in a variety of applications such as design of soundproofing walls, invisible cloths and aeroplanes, and seismic cloaks for earthquake damage mitigation. Both experimental and theoretical investigations on the elastic/acoustic wave propagation in phononic crystals are carried out during the last decades. Experiments on phonotic crystals with a large number of periodical structures are difficult to conduct; they are also unnecessary when the materials are elastic and theoretical or numerical solutions are available [3, 4]. This paper will focus on numerical modelling of the behavior of phonotic crystals subjected to acoustic pressure waves.

Many numerical methods have been used to compute the band structures and bandgaps of phononic crystals, as experiments are often too delicate or complicated to undertake and control. However, most of the existing numerical methods cannot efficiently tackle this problem. For example, in the most popular finite element method (FEM), the numerical integration of periodic boundary conditions is often very time consuming [5, 6]. The plane wave expansion and the wavelet method neglect transverse waves in solids which may result in numerical errors [7-10]. The multi-scattering theory method [11, 12] and the Dirichlet-to-Neumann map method [13-15] are limited for scatterers with circle or sphere shapes. The boundary element method (BEM) involves singular integrals and may result in unreal, fictitious eigenfrequencies [16-20]. The generalized multipole techniques [21-23] are computationally very demanding because the band structure can only be obtained from the time domain using the Fast Fourier Transform method at the present. The time-domain finite difference approach [24, 25] can consider different wave

*Corresponding author, Tel.: +44 7557425754, Email: ac1098@coventry.ac.uk

modes in solids and fluids but often has to neglect solid-fluid interactions at the interfaces. In addition, most of the existing numerical simulations deal with 2D problems of phonotic crystals only, with a few 3D exceptions such as [26, 27]. Therefore, accurate and efficient numerical methods are still needed to compute the band structures of phononic crystals, especially for 3D cases.

The radial basis function collocation method (RBFCM) implemented in the meshless framework has been under development since 1990s [28-29]. Due to the full matrix formulation in the RBFCM, the local collocation approach, also known as the RBF-FD method or local RBFCM (LRBFCM), was introduced in 2000s [30-35]. The LRBFCM method is dimensional free and is easy to implement. However, the instability problem caused by the Neumann boundary conditions still limits its wider applications considerably [36-37]. Special treatments such as the direct method [36], the least square method [39], and the fictitious node method [40-42] were subsequently introduced to calculate the derivatives of primary field quantities (e.g., sound wave pressure), allowing for more stable computation of the band structures of phononic crystals. However, the LRBFCM has been applied to 2D phononic crystals only.

In our previous study [43], an LRBFCM-based approach was proposed for calculating band structures of 2D phononic crystals. The approach is unique in that only one fictitious node is used for computation of derivatives so that the continuity condition between material interfaces is satisfied with high numerical stability and efficiency. In this work, we further extend the LRBFCM in [43] from 2D to 3D phononic crystals by re-formulating the computing algorithm for derivatives in 3D. The method is validated by simulation of benchmark examples with sound pressure wave propagation and result comparisons with finite element modelling. The paper is organized as follows. The problem of 3D phononic crystals is briefly introduced in section 2, followed by a detailed presentation of the general formulation and solutions of LRBFCM in section 3. Numerical results of examples with different materials and scatterers are then presented and discussed in section 4, with main conclusions given in the last section.

2. The problem of 3D phononic crystals

In this section, the governing equations, interface continuity conditions, and periodic boundary conditions of 3D phononic crystals under sound pressure waves are briefly presented for the convenience of discussion as follows. A unit cell composed of a cube scatterers embedded in a cube matrix with the lattice constant a is illustrated in Fig. 1a, where Γ_1 to Γ_6 represent the six faces of the cube, with Γ_1 and Γ_2 perpendicular to $\boldsymbol{x}$ axis, Γ_3 and Γ_4 to $\boldsymbol{y}$ axis, and Γ_5 and Γ_6 to z axis, respectively. Γ_0 denotes the interface between the matrix and scatterer. The first Brillouin zone is shown in Fig. 1b.

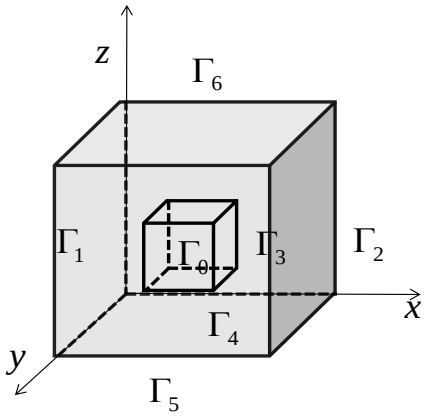

(a) A cube unit cell

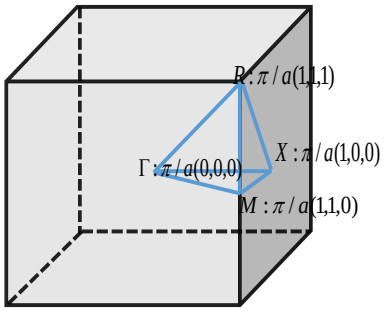

(b) The first Brillouin zone

Fig. 1 A cubic phononic crystal

2.1 Governing equations

The governing equations of the sound pressure waves in a homogeneous, isotropic and linear elastic solid are

$$\Delta p(\boldsymbol{x}) = -\frac{\omega^2}{c^2} p(\boldsymbol{x}), \tag{1}$$

where ω is the rotation frequency, $c = \sqrt{K/\rho}$ the wave speed, ρ the mass density, p the pressure, and K the bulk modulus. The operator Δ is Laplace operator.

2.2 Interface continuity conditions

The continuity conditions on the interface Γ_0 are expressed as

$$p_1(\boldsymbol{x}) = p_2(\boldsymbol{x}), \qquad \boldsymbol{x} \in \Gamma_0, \tag{2}$$

$$\frac{\partial p_1(\boldsymbol{x})}{\partial \boldsymbol{n}} = \frac{\partial p_2(\boldsymbol{x})}{\partial \boldsymbol{n}}, \qquad \boldsymbol{x} \in \Gamma_0, \tag{3}$$

where $\boldsymbol{n} = \left(n_x, n_y, n_z\right)^T$ is the outward unit normal vector of the interface, and the supersc ript 1 denotes the matrix domain D_1 and 2 the scatterer domain D_2.

2.3 Periodic boundary conditions

The periodic boundary conditions are given as

$$p(\boldsymbol{x} + \boldsymbol{a}) = e^{i\boldsymbol{k}\cdot\boldsymbol{a}} p(\boldsymbol{x}), \tag{4}$$

$$\frac{\partial p}{\partial \boldsymbol{n}}(\boldsymbol{x} + \boldsymbol{a}) = e^{i\boldsymbol{k}\cdot\boldsymbol{a}} \frac{\partial p(\boldsymbol{x})}{\partial \boldsymbol{n}}, \tag{5}$$

where $\boldsymbol{k} = (k_x, k_y, k_z)^T$ is the Bloch wave vector, $i = \sqrt{-1}$, and $\boldsymbol{a} = l_1\boldsymbol{a}_1 + l_2\boldsymbol{a}_2 + l_3\boldsymbol{a}_3$ with $(l_1, l_2, l_3) \in \mathrm{Z}^2$, where $\boldsymbol{a}_1$, $\boldsymbol{a}_2$ and $\boldsymbol{a}_3$ are fundamental translation vectors of the lattices. For the cubic lattice we have

$$p(\boldsymbol{x}_{\Gamma_1} + \boldsymbol{a}) = e^{ik_x a} p(\boldsymbol{x}_{\Gamma_2}), \quad p(\boldsymbol{x}_{\Gamma_3} + \boldsymbol{a}) = e^{ik_y a} p(\boldsymbol{x}_{\Gamma_4}), \quad p(\boldsymbol{x}_{\Gamma_5} + \boldsymbol{a}) = e^{ik_z a} p(\boldsymbol{x}_{\Gamma_6}), \tag{6}$$

and

$$\frac{\partial p}{\partial x}(\boldsymbol{x}_{\Gamma_1}+\boldsymbol{a})=e^{ik_x a}\frac{\partial p(\boldsymbol{x}_{\Gamma_2})}{\partial x}, \quad \frac{\partial p}{\partial y}(\boldsymbol{x}_{\Gamma_3}+\boldsymbol{a})=e^{ik_y a}\frac{\partial p(\boldsymbol{x}_{\Gamma_4})}{\partial y}, \quad \frac{\partial p}{\partial z}(\boldsymbol{x}_{\Gamma_5}+\boldsymbol{a})=e^{ik_z a}\frac{\partial p(\boldsymbol{x}_{\Gamma_6})}{\partial z}, \tag{7}$$

where $\boldsymbol{x}_{\Gamma_i}$ (i=1~6) are the nodes on the boundaries Γ_i.

3. Numerical discretization of LRBFCM

In this section, the details of the LRBFCM formulation, derivative calculation, and numerical discretization for 3D phononic crystals are fully presented.

3.1 General formulation of LRBFCM

The general solution of the wave pressure p can be approximated by

$$p(\boldsymbol{x})=\sum_{m=1}^{N_s}\varphi\left(\left\|\boldsymbol{x}-\boldsymbol{x}_m\right\|\right)\alpha_m, \tag{8}$$

where N_s is the total number of local nodes, φ the radial basis functions (RBF), and α_m the unknown coefficient related to $u(\boldsymbol{x}_m)$ of the local node at $\boldsymbol{x}_m$, which can be calculated by

$$\boldsymbol{\alpha}_m=\boldsymbol{\varphi}^{-1}\overline{\boldsymbol{p}}, \tag{9}$$

where $\overline{\boldsymbol{p}}=[p(\boldsymbol{x}_1),...,p(\boldsymbol{x}_m)]^T$ is the vector of the pressure of the local nodes, the subscript m denotes the mth element of a vector, namely, at the mth node $\boldsymbol{x}=\boldsymbol{x}_m\cdot\boldsymbol{\alpha}_m=[\alpha_1,\alpha_2,...,\alpha_m]^T$ is the vector of unknown coefficients, and $\boldsymbol{\varphi}=\left[\boldsymbol{\varphi}\left(\left\|\boldsymbol{x}_j-\boldsymbol{x}_l\right\|\right)\right]_{1\le l,\,j\le N_s}$ is the RBF interpolation matrix with the size of $N_s\times N_s$. Considering Eq. (9), Eq. (8) can be expressed as

$$p(\boldsymbol{x})=\sum_{m=1}^{N_s}\varphi\left(\left\|\boldsymbol{x}-\boldsymbol{x}_m\right\|\right)\alpha_m=\Theta\boldsymbol{\varphi}^{-1}\overline{\boldsymbol{p}}, \tag{10}$$

where

$$\Theta=\left[\varphi\left(\left\|\boldsymbol{x}-\boldsymbol{x}_1\right\|\right),...,\varphi\left(\left\|\boldsymbol{x}-\boldsymbol{x}_{N_s}\right\|\right)\right]. \tag{11}$$

In Eq. (10), $\Theta\boldsymbol{\varphi}^{-1}$ is the vector with the size of N_s related to local nodes. For convenience, the following definition is introduced

$$\overline{\boldsymbol{\varphi}}(\boldsymbol{x})=\Theta(\boldsymbol{x})\boldsymbol{\varphi}^{-1}. \tag{12}$$

The wave pressure given in Eq. (10) becomes

$$p(\boldsymbol{x})=\overline{\boldsymbol{\varphi}}(\boldsymbol{x})\overline{\boldsymbol{p}}. \tag{13}$$

From Eq. (13), it is easy to reformulate the vector $\overline{\boldsymbol{\varphi}}(\boldsymbol{x})$ to a global vector by inserting zeros at

proper positions. For simplicity, two global vectors $\tilde{\boldsymbol{\varphi}}(\boldsymbol{x})$ and $\tilde{\boldsymbol{p}}$ with the size of N (the number of global nodes) are defined by mapping the local ones with the size of N_s as

$$\begin{aligned} &\text{local } \bar{\boldsymbol{\varphi}}(\boldsymbol{x}) \quad \Rightarrow \quad \text{global } \tilde{\boldsymbol{\varphi}}(\boldsymbol{x}), \\ &\text{local } \bar{\boldsymbol{p}} \qquad \Rightarrow \quad \text{global } \tilde{\boldsymbol{p}}, \end{aligned} \tag{14}$$

where $\tilde{\boldsymbol{p}} = \left[p(\boldsymbol{x}_1), ..., p(\boldsymbol{x}_N) \right]^T$ is the vector of field quantities in the global domain. The global vector $\tilde{\boldsymbol{\varphi}}(\boldsymbol{x}) = [\tilde{\varphi}_1(\boldsymbol{x}), ..., \tilde{\varphi}_N(\boldsymbol{x})]$ is a sparse vector related to the local vector. Using the relationships (14), Eq. (13) can be expressed as

$$p(\boldsymbol{x}) = \bar{\boldsymbol{\varphi}}(\boldsymbol{x}) \bar{\boldsymbol{p}} = \tilde{\boldsymbol{\varphi}}(\boldsymbol{x}) \tilde{\boldsymbol{p}}, \tag{15}$$

where the unknown wave pressure vector $\tilde{\boldsymbol{p}}$ can be determined from the governing partial differential equations and boundary conditions. $\bar{\boldsymbol{\varphi}}(\boldsymbol{x})$ is related to the the partial differentiation of $\Theta(\boldsymbol{x})$ while $\boldsymbol{\varphi}^{-1}$ is a constant matrix, i.e.,

$$\frac{\partial p(\boldsymbol{x})}{\partial x_i} = \frac{\partial \tilde{\boldsymbol{\varphi}}(\boldsymbol{x})}{\partial x_i} \tilde{\boldsymbol{p}} \Rightarrow \quad \frac{\partial \bar{\boldsymbol{\varphi}}(\boldsymbol{x})}{\partial x_i} \bar{\boldsymbol{p}} = \frac{\partial \Theta(\boldsymbol{x})}{\partial x_i} \boldsymbol{\varphi}^{-1} \bar{\boldsymbol{p}}, \tag{16}$$

It is clear that

$$p(x_m) = \tilde{\boldsymbol{\varphi}}(\boldsymbol{x}_m) \tilde{\boldsymbol{p}} = \sum_{k=1}^{N} \tilde{\varphi}_k(\boldsymbol{x}_m) p(\boldsymbol{x}_k) = \sum_{k=1}^{N} \delta_{km} p(\boldsymbol{x}_k) = p(\boldsymbol{x}_m), \tag{17}$$

therefore the functions $\tilde{\boldsymbol{\varphi}}(\mathbf{x})$ obey the Kronecker-delta property, namely, $\tilde{\varphi}_k(\boldsymbol{x}_m) = \delta_{km}$ or $\tilde{\boldsymbol{\varphi}}(\boldsymbol{x}_m) = \left[\tilde{\varphi}_1(\boldsymbol{x}_m) = 0, ..., \tilde{\varphi}_m(\boldsymbol{x}_m) = 1, ..., \tilde{\varphi}_N(\boldsymbol{x}_m) = 0 \right]$.

3.2 Calculation of derivatives

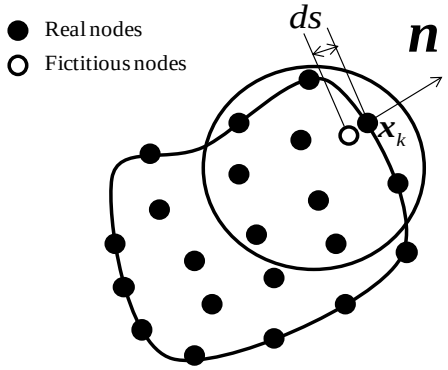

Fig. 2 The improved fictitious node method

The derivative calculation is one of the main reasons for the instability of the LRBFCM. The

derivative form of the RBF is not only related to the Euclidean distance but also to the direction of local nodes. Herein only one fictitious node is interpolated using the local nodes within a certain distance, as shown in Fig. 2. Then the derivative can be formulated using a finite difference form by subtracting the field quantity of the closest node $\boldsymbol{x}_k$. The derivative of the field quantity can be expressed as

$$\frac{\partial u(\boldsymbol{x})}{\partial \boldsymbol{n}} = \frac{u(\boldsymbol{x}) - u(\tilde{\boldsymbol{x}})}{ds}, \tag{18}$$

where ds is the distance between the closest node and the fictitious node, as shown in Fig. 2. Considering Eq. (15), Eq. (18) can be rewritten as

$$\frac{\partial u(\boldsymbol{x})}{\partial \boldsymbol{n}} = \frac{u(\boldsymbol{x}) - u(\tilde{\boldsymbol{x}})}{ds} = \frac{\tilde{\boldsymbol{\varphi}}(\boldsymbol{x}) - \tilde{\boldsymbol{\varphi}}(\tilde{\boldsymbol{x}})}{ds} \boldsymbol{u}_{N_s}. \tag{19}$$

As $\tilde{\boldsymbol{\varphi}}(\boldsymbol{x})$ has the Kronecker-delta property $\tilde{\varphi}_k(\boldsymbol{x}_m) = \delta_{km}$, Eq. (19) can be modified as

$$\frac{\tilde{\boldsymbol{\varphi}}(\tilde{\boldsymbol{x}}) - \tilde{\boldsymbol{\varphi}}(\boldsymbol{x})}{ds} = \frac{\left[\tilde{\varphi}_1(\tilde{\boldsymbol{x}}), ..., \tilde{\varphi}_k(\tilde{\boldsymbol{x}}) - 1, ..., \tilde{\varphi}_N(\boldsymbol{x})\right]}{ds}, \tag{20}$$

where k denotes the node $\boldsymbol{x}_k$ as shown in Fig. 3. In Eq. (20), the field quantity of the only fictitious node is interpolated using the local nodes in the small domain. The field quantity at the boundary node is given analytically in the derivative calculation, whose accuracy is only dependent on the interpolation of the field quantity at the fictitious node. The above method has proven to be highly accurate and stable for 2D phonotic crystal problems [43], and it will be further tested for modelling 3D problems as below.

3.3 Band structure computation of phononic crystals

Eq. (1), Eq. (3), and Eq. (7) can be written in the following matrix form

$$\begin{bmatrix} \Delta \boldsymbol{p}(\boldsymbol{x}^2) & \boldsymbol{0} \\ \boldsymbol{0} & \Delta \boldsymbol{p}(\boldsymbol{x}^1) \\ \dfrac{\partial \boldsymbol{p}(\boldsymbol{x}_{\Gamma_1})}{\partial x} - \dfrac{\partial \boldsymbol{p}(\boldsymbol{x}_{\Gamma_2})}{\partial x} e^{-ik_x a} & \boldsymbol{0} \\ \dfrac{\partial \boldsymbol{p}(\boldsymbol{x}_{\Gamma_3})}{\partial y} - \dfrac{\partial \boldsymbol{p}(\boldsymbol{x}_{\Gamma_4})}{\partial y} e^{-ik_y a} & \boldsymbol{0} \\ \dfrac{\partial \boldsymbol{p}(\boldsymbol{x}_{\Gamma_5})}{\partial z} - \dfrac{\partial \boldsymbol{p}(\boldsymbol{x}_{\Gamma_6})}{\partial z} e^{-ik_z a} & \boldsymbol{0} \\ \dfrac{\partial \boldsymbol{p}(\boldsymbol{x}^0_{\Gamma_0})}{\partial \boldsymbol{n}} & -\dfrac{\partial \boldsymbol{p}(\boldsymbol{x}^1_{\Gamma_0})}{\partial \boldsymbol{n}} \end{bmatrix} = -\omega^2 \begin{bmatrix} \dfrac{\rho_2}{K_2} \boldsymbol{p}(\boldsymbol{x}^2) & \boldsymbol{0} \\ \boldsymbol{0} & \dfrac{\rho_1}{K_1} \boldsymbol{p}(\boldsymbol{x}^1) \\ \boldsymbol{0} & \boldsymbol{0} \\ \boldsymbol{0} & \boldsymbol{0} \\ \boldsymbol{0} & \boldsymbol{0} \\ \boldsymbol{0} & \boldsymbol{0} \end{bmatrix}, \tag{21}$$

where $\boldsymbol{x}^1 \in D_1$, $\boldsymbol{x}^2 \in D_2$ and $\boldsymbol{x}_{\Gamma_i} \in \Gamma_i$ (i=0,1,...,6). The following generalized eigenvalue matrix can be formulated by substituting Eq. (15) into Eq. (21)

$$\begin{bmatrix} \Delta\tilde{\boldsymbol{\varphi}}(\boldsymbol{x}^2) & \mathbf{0} \\ \mathbf{0} & \Delta\tilde{\boldsymbol{\varphi}}(\boldsymbol{x}^1) \\ \dfrac{\partial\tilde{\boldsymbol{\varphi}}(\boldsymbol{x}_{\Gamma_1})}{\partial x}-\dfrac{\partial\tilde{\boldsymbol{\varphi}}(\boldsymbol{x}_{\Gamma_2})}{\partial x}e^{-ik_x a} & \mathbf{0} \\ \dfrac{\partial\tilde{\boldsymbol{\varphi}}(\boldsymbol{x}_{\Gamma_3})}{\partial y}-\dfrac{\partial\tilde{\boldsymbol{\varphi}}(\boldsymbol{x}_{\Gamma_4})}{\partial y}e^{-ik_y a} & \mathbf{0} \\ \dfrac{\partial\tilde{\boldsymbol{\varphi}}(\boldsymbol{x}_{\Gamma_5})}{\partial z}-\dfrac{\partial\tilde{\boldsymbol{\varphi}}(\boldsymbol{x}_{\Gamma_6})}{\partial z}e^{-ik_z a} & \mathbf{0} \\ \dfrac{\partial\boldsymbol{p}(\boldsymbol{x}^0_{\Gamma_0})}{\partial\boldsymbol{n}} & -\dfrac{\partial\boldsymbol{p}(\boldsymbol{x}^1_{\Gamma_0})}{\partial\boldsymbol{n}} \end{bmatrix} \begin{bmatrix} \tilde{\boldsymbol{p}}^2 \\ \tilde{\boldsymbol{p}}^1 \end{bmatrix} = -\omega^2 \begin{bmatrix} \dfrac{\rho_2}{K_2}\tilde{\boldsymbol{\varphi}}(\boldsymbol{x}^2) & \mathbf{0} \\ \mathbf{0} & \dfrac{\rho_1}{K_1}\tilde{\boldsymbol{\varphi}}(\boldsymbol{x}^1) \\ \mathbf{0} & \mathbf{0} \\ \mathbf{0} & \mathbf{0} \\ \mathbf{0} & \mathbf{0} \\ \mathbf{0} & \mathbf{0} \end{bmatrix} \begin{bmatrix} \tilde{\boldsymbol{p}}^2 \\ \tilde{\boldsymbol{p}}^1 \end{bmatrix}, \quad (22)$$

where $\tilde{\boldsymbol{p}}^2$ and $\tilde{\boldsymbol{p}}^1$ are the pressure vectors in D_1 and D_2, respectively.

Eq. (19) can be re-written as

$$\boldsymbol{AP} = -\omega^2 \boldsymbol{BP}, \quad (23)$$

By re-ordering the nodes, the matrix $\boldsymbol{A}$, $\boldsymbol{B}$ and $\boldsymbol{P}$ can be expressed in terms of columns corresponding to the domain D_1, D_2 and the boundary $\Gamma_i (i = 0,1...6)$ as, respectively

$$\boldsymbol{A} = \left[\boldsymbol{A}^0, \boldsymbol{A}_{\Gamma_1}, \boldsymbol{A}_{\Gamma_2}, \boldsymbol{A}_{\Gamma_3}, \boldsymbol{A}_{\Gamma_4}, \boldsymbol{A}_{\Gamma_5}, \boldsymbol{A}_{\Gamma_6}, \boldsymbol{A}^0_{\Gamma_0}, \boldsymbol{A}^1, \boldsymbol{A}^1_{\Gamma_0} \right],$$

$$\boldsymbol{B} = \left[\boldsymbol{B}^0, \boldsymbol{B}_{\Gamma_1}, \boldsymbol{B}_{\Gamma_2}, \boldsymbol{B}_{\Gamma_3}, \boldsymbol{B}_{\Gamma_4}, \boldsymbol{B}_{\Gamma_5}, \boldsymbol{B}_{\Gamma_6}, \boldsymbol{B}^0_{\Gamma_0}, \boldsymbol{B}^1, \boldsymbol{B}^1_{\Gamma_0} \right],$$

$$\boldsymbol{P} = \left[\boldsymbol{P}^0, \boldsymbol{P}_{\Gamma_1}, \boldsymbol{P}_{\Gamma_2}, \boldsymbol{P}_{\Gamma_3}, \boldsymbol{P}_{\Gamma_4}, \boldsymbol{P}_{\Gamma_5}, \boldsymbol{P}_{\Gamma_6}, \boldsymbol{P}^0_{\Gamma_0}, \boldsymbol{P}^1, \boldsymbol{P}^1_{\Gamma_0} \right]^T.$$

The interface condition Eq. (2) and the periodic boundary condition Eq. (6) are considered analytically in the generalized eigenvalue matrix form by adding or subtracting the relevant columns, which leads to

$$\bar{\boldsymbol{A}}\bar{\boldsymbol{P}} = -\omega^2 \bar{\boldsymbol{B}}\bar{\boldsymbol{P}} \quad (24)$$

where

$$\bar{\boldsymbol{A}} = \left[\boldsymbol{A}^0, \boldsymbol{A}^1, \boldsymbol{A}_{\Gamma_1} + \boldsymbol{A}_{\Gamma_2} e^{ik_x a}, \boldsymbol{A}_{\Gamma_3} + \boldsymbol{A}_{\Gamma_4} e^{ik_y a}, \boldsymbol{A}_{\Gamma_5} + \boldsymbol{A}_{\Gamma_6} e^{ik_z a}, \boldsymbol{A}^0_{\Gamma_0} + \boldsymbol{A}^1_{\Gamma_0} \right],$$

$$\bar{\boldsymbol{B}} = \left[\boldsymbol{B}^0, \boldsymbol{B}^1, \boldsymbol{B}_{\Gamma_1} + \boldsymbol{B}_{\Gamma_2} e^{ik_x a}, \boldsymbol{B}_{\Gamma_3} + \boldsymbol{B}_{\Gamma_4} e^{ik_y a}, \boldsymbol{B}_{\Gamma_5} + \boldsymbol{B}_{\Gamma_6} e^{ik_z a}, \boldsymbol{B}^0_{\Gamma_0} + \boldsymbol{B}^1_{\Gamma_0} \right],$$

$$\bar{\boldsymbol{P}} = \left[\boldsymbol{P}^0, \boldsymbol{P}^1, \boldsymbol{P}_{\Gamma_1}, \boldsymbol{P}_{\Gamma_2}, \boldsymbol{P}_{\Gamma_3}, \boldsymbol{P}^0_{\Gamma_0} \right]^T.$$

The formulated matrices in Eq. (24) are sparse and symmetric. Then eigenvalues are obtained by solving Eq. (24) with corresponding wave vectors [k_x, k_y , k_z] varing from R→M→Γ→X→M in the first Brillouin zone, as shown in Fig.1(b). The band structure can then be plotted by putting all these eigenfrequencies together, to describe the passing ability of the pressure wave with respect to different directions [k_x, k_y , k_z] in the periodical structures.

The main steps of calculating the band structure using the above method is briefly summarized in

Fig. 3.

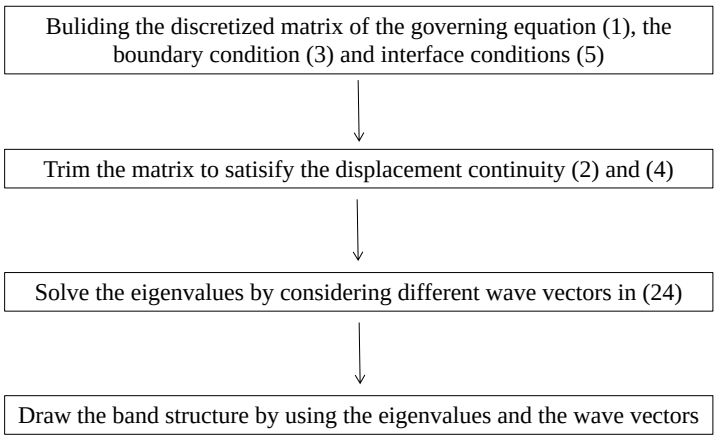

Fig. 3 The main steps of calculating the band structure using the developed method

4. Examples, results and discussion

The 3D phonotic crystals of cube matrix / cube scatterer (Fig. 1) and cube matrix / sphere scatterer with different material properties under sound wave pressure are simulated as benchmark problems to validate the above developed LRBFCM method, which is implemented in an in-house Matlab code. They are also modelled by FEM using COMSOL^{TM} Multiphysics for comparison of accuracy and efficiency. All the simulations are run on a desktop PC with Intel(R) Core(TM) i9-7940X, 3.10 GHz CPU and 128 GB RAM. In the LRBFCM simulations, the multi-quadric (MQ) RBF [41] is used,

$$\varphi = \sqrt{r^2 + c_s^{\,2}} \tag{25}$$

where $r = \left\| \boldsymbol{x} - \boldsymbol{x}_n \right\|$ is the Euclidean distance and c_s is a chosen shape parameter. The optimal value of shape parameter is dependent on the form of RBF and the nodal distance or the number of local nodes. In the present work, c_s =1 with 9 local nodes is found by trial and error to result in a smooth error distribution in the analyzed domain. A uniform nodal distribution is used as it often has better convergence rates than a random one of equal distance [39-43]. The generalized eigenvalue equation Eq. (24) is solved directly using the function *eigs* in Matlab. The simulation of FEM is carried out by using commercial software COMSOL 5.0.

4.1 Example of a special case

In order to validate the accuracy of the proposed method, a 0.4×0.4×0.4 scatterer embedded in a 1×1×1 cubic unit cell is modelled first, but with the same material for the scatterer and the inclusion. For this special case, there exists an analytical dispersion relation [44]:

$$\omega(k) = \sqrt{(k-m)^2 + n^2 + q^2}\,, \tag{26}$$

where m = 0, ±1, ±2, …; n and q = 1, 2, 3, ….

Fig. 4 compares the band structures calculated from the RBF(in red line) and Eq. 26 (in blue dot). The relative error is defined as

$$Errors = \sum \left| E_r - E_f \right| / \sum \left| E_f \right|, \tag{27}$$

where E_f is the result from the FEM or exact solutions, and E_r from the LRBFCM. The relative error for this example is only 0.0042, demonstrating high accuracy of the developed method.

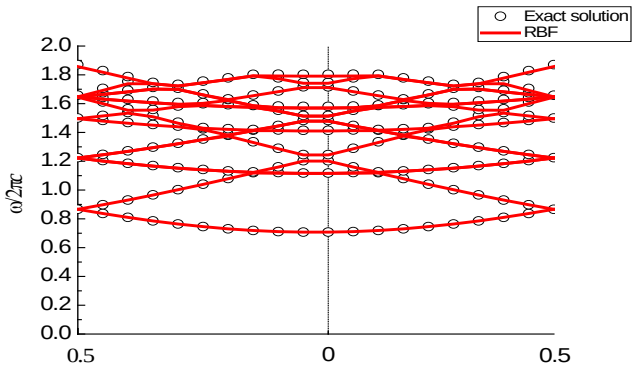

Fig. 4 A comparison between the RBF and exact solutions

4.2 Cube/Cube examples

A 0.4×0.4×0.4 scatterer embedded in a 1×1×1 cubic unit cell is modeled first, and 41 wave vector nodes are employed from R→M→Γ→X→M to obtain the band structure, as shown in Fig. 1b. 21×21×21=9261 nodes with 9261 degrees of freedoms (DOFs) are uniformly distributed in the whole domain for the LRBFCM, and a very fine mesh with 15,426 triangle elements and 22,199 DOFs is used in FEM as the "accurate" reference for comparison.

In order to demonstrate the robustness of the proposed method, iron scatterers embedded in mercury, water and air matrix are modelled, respectively. The material constants are ρ_1=13600kg/m^3 and c_1=1450m/s for mercury, ρ_1=1000kg/m^3 and c_1=1499m/s for water, ρ_1=1.21kg/m^3 and c_1=340m/s for air, and ρ_2=7870kg/m^3 and c_2=5000m/s for iron.

The modelled band structures for different matrix materials are shown in Figs 5-7. It is clear that the present results agree very well with the FEM results. The differences are negligible for low frequencies and appear to increase at higher frequencies as the differences in material properties of scatterer and matrix increase (from Fig. 5 to Fig. 7).

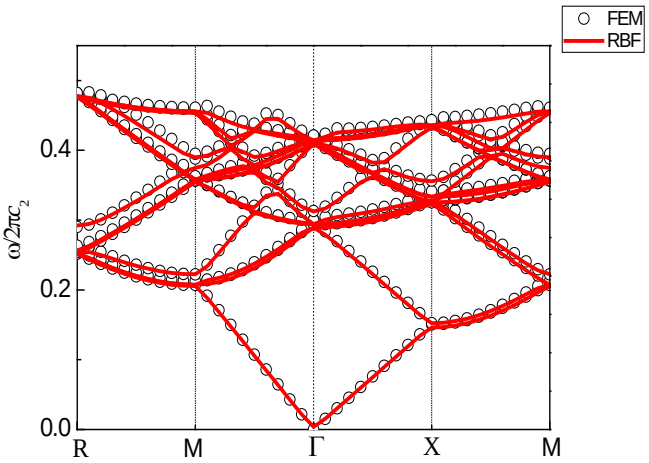

Fig. 5 Band structures of iron scatterer embedded in mercury matrix

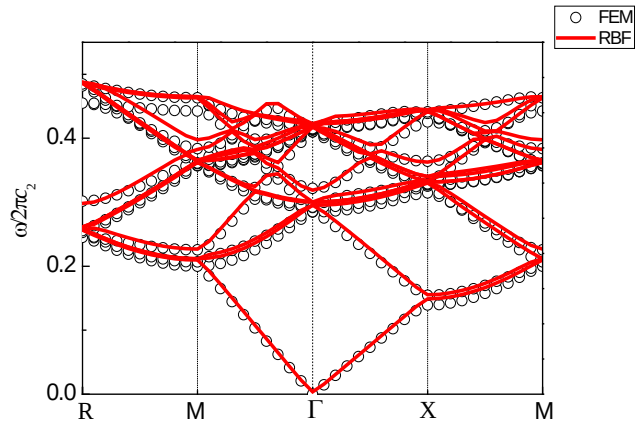

Fig. 6 Band structures of iron scatterer embedded in water matrix

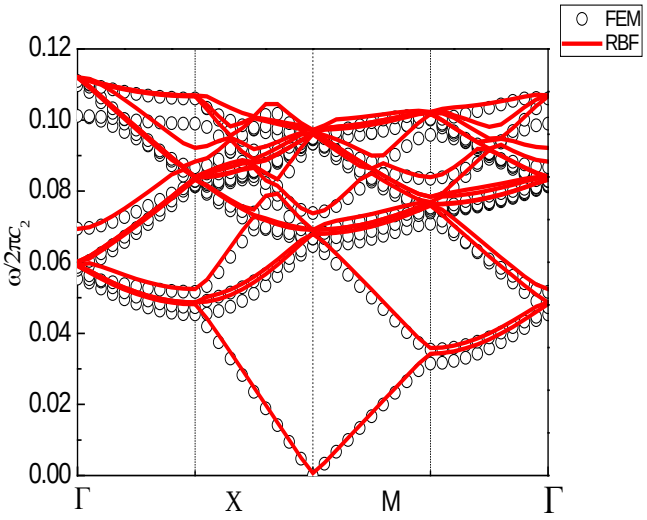

Fig. 7 Band structures of iron scatterer embedded in air matrix

The CPU times and errors of the results from the FEM and the LRBFCM for the above examples are compared in Table 1.

It can be seen that the LRBFCM performs much more efficiently than the FEM but with negligible differences. The computing time is much less than that required by the FEM, with more than 35% savings in all the cases considered. The time saving would be even more significant if more wave vectors are considered. The high efficiency of the present LRBFCM is attributed to the fact that it is based on a strong-form formulation of partial differential equations and does not need any numerical integration for computing the system matrices. It can also be noted that the errors become higher as the difference between two materials the properties increases. As there is no exact solution, the error is just a relative indicator showing which mesh or method is more accurate.

Table 1 Comparisons of computing time and accuracy for cube/cube examples

Materials		**Iron/Air**	**Iron/Water**	**Iron/Mercury**
RBF	Degrees of freedom	9262		
	CPU time (s)	143.6	142.9	140.6
FEM	Degrees of freedom	9293		
	CPU time (s)	221	220	217
Comparison	Errors	3.25%	0.21%	0.20%
	Time saving	35.02%	35.03%	35.21%

4.3 Cube/Sphere examples

A 0.3 radial sphere scatterer embedded in a 1×1×1 cubic unit cell is considered in this part, and the same wave vector nodes are employed from R→M→Γ→X→M to obtain the band structure, as shown in Fig. 1b. In total, 9639 nodes with the same number of DOFs are distributed in the whole domain for the LRBFCM, and a mesh with 16,008 triangle elements and 22979 DOFs are used in FEM for comparison.

The band structures of phononic crystals with the same materials for the above cube/cube examples are shown in the Appendix. Again the results from the developed method and the FEM match each other very well, even for high frequencies and very different scatter/matrix materials.

The computational performances are compared in Table 2. Again the new LRBFCM is more efficient than the FEM with more than 30% savings in the CPU times. However the errors in Table 2 are higher than those in Table 1. This is due to the different interfaces in the two examples. In the cubic/cubic example, the interface is a cubic surface, which the FEM can deal with as well as the developed method. However, in the cubic/sphere example, the interface is a sphere, and the FEM struggles to model the curved geometry accurately due to the difficulty in mesh generation. On the contrary, the developed meshless method can simulate both interfaces easily and accurately. The errors become lower when finer meshes are used, for example, the error in the case of Iron embedded in Mercury is 1.72% when 44459 DOFs are used in FEM for the Cube/Sphere example.

5. Conclusions

In this paper, the new LRBFCM developed for 2D phononic crystals [43] has been further extended to calculate the band structure of 3D cases. Numerical results from modelling a number of benchmark examples show that the method is capable of efficiently and accurately computing the band structure of 3D phononic crystals, due to its advantages in dealing with complicated boundary or interface shapes and calculating derivatives of field quantities. The improved LRBFCM can be extended to simulate other problems such as acoustics, solid-fluid interaction, crack propagation and hydrodynamics with moving boundaries.

Table 2 Comparisons of computing time and accuracy for Cube/Sphere examples

Materials		**Air/Iron**	**Water/Iron**	**Mercury/Iron**
RBF	Degrees of freedom	9639		
	Time spent [s]	148.3	147.5	149.5
FEM	Degrees of freedom	9538		
	Time spent [s]	212	225	219
Comparison	Errors	4.49%	3.36%	3.25%
	Time saving	30.05%	34.44%	31.47%

Acknowledgement

This work was first undertaken as part of a Postdoctoral Fellowship (H. Zheng) at Coventry University and subsequently developed under a National Natural Science Foundation of China grant (No: 11702125). H. Zheng would also like to acknowledge the support from the Double Thousand Talents Plan of Jiangxi Province.

Appendix

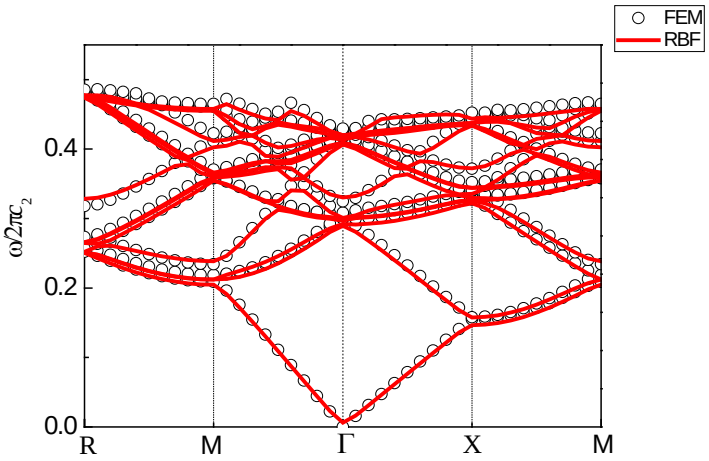

A.1 Band structure of Iron embedded in Mercury

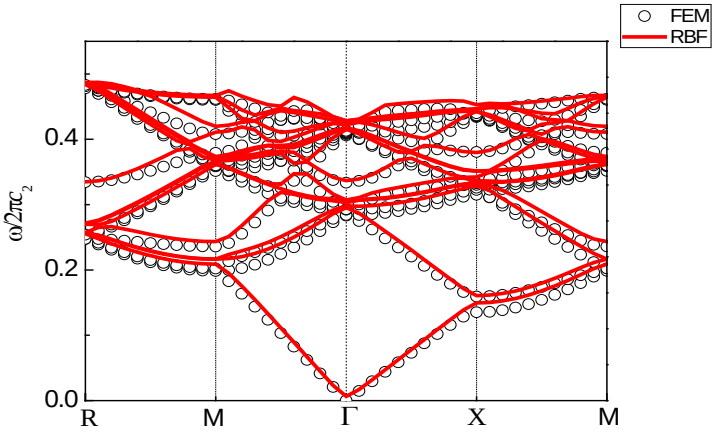

A.2 Band structure of Iron embedded in Water

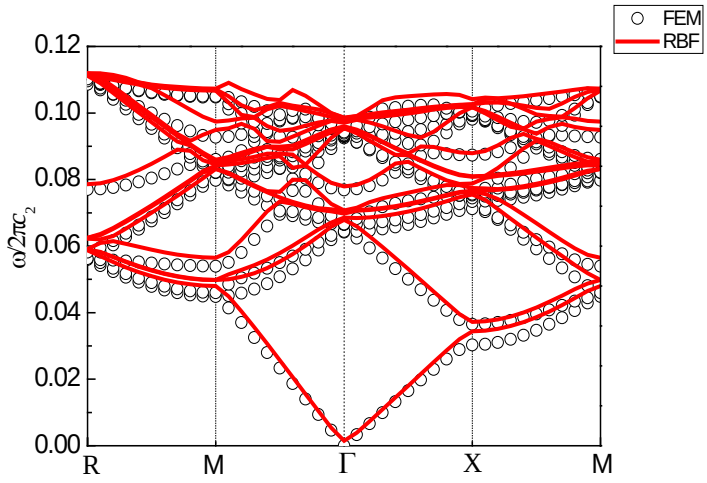

A.3 Band structure of Iron embedded in Air

References

[1] Kushwaha MS, Halevi P, Dobrzynski L, Djafarirouhani B. Acoustic band-structure of periodic elastic composites. Physical Review Letters 1993; 71(13): 2022-2025.

[2] Hou G, Wang J, Layton A. Numerical methods for fluid-structure interaction - A review. Communications in Computational Physics 2012; 12(2): 337-377.

[3] Liu ZY, Zhang X, Mao Y, Zhu YY, Yang Z, Chan CT, Sheng P. Locally Resonant Sonic Materials. 2000; 289(5485): 1734-1736.

[4] Lucklum F, Vellekoop MJ. Rapid Prototyping of 3D Phononic Crystals using High-resolution Stereolithography Fabrication. Procedia Engineering 2015; 120: 1095-1098.

[5] Li E, He Z C, Hu J Y, et al. Volumetric locking issue with uncertainty in the design of locally resonant acoustic metamaterials. Computer Methods in Applied Mechanics & Engineering, 2017, 324.

[6] Belytschko T, Liu WK, Moran B, Elkhodary K. Nonlinear Finite Elements for Continua and Structures (second edition). In: John Wiley & Sons, Ltd, West Sussex, 2014.

[7] Cao YJ, Hou ZL, Liu YY. Convergence problem of plane-wave expansion method for phononic crystals. Physics Letters A 2004; 327(2-3): 247-253.

[8] Wu TT, Huang ZG, Lin S. Surface and bulk acoustic waves in two-dimensional phononic crystal consisting of materials with general anisotropy. Physical Review B 2004;69(9): 094301(1)-094301(10).

[8] Yan ZZ, Wang YS. Wavelet-based method for calculating elastic band gaps of two-dimensional phononic crystals. Physical Review B 2006; 74(22): 622-630.

[9] Checoury X, Lourtioz JM. Wavelet method for computing band diagrams of 2D photonic crystals. Optics Communications 2006; 259(1): 360-365.

[10] Sigalas MM, García N. Importance of coupling between longitudinal and transverse components for the creation of acoustic band gaps: The aluminum in mercury case. Applied Physics Letters 2000; 76(16): 2307-2309.

[11] Sigalas MM, Economou EN. Elastic and acoustic-wave band structure. Journal of Sound and Vibration 1992; 158(2): 377-382.

[12] Kafesaki M, Economou EN. Multiple-scattering theory for three-dimensional periodic acoustic composites. Physical Review B 1999;60(17): 11993-2001.

[13] Wu YM, Lu YY. Dirichlet-to-Neumann map method for analyzing interpenetrating cylinder arrays in a triangular lattice. Journal of the Optical Society of America B 2008;25(9): 1466-1473.

[14] Li FL, Wang YS, Zhang CZ. Bandgap calculation of two-dimensional mixed solid-fluid phononic crystals by Dirichlet-to-Neumann maps. Physica Scripta 2011;84(5): 055402-55410.

[15] Zhen N, Li FL, Wang YS, Zhang CZ. Bandgap calculation for mixed in-plane waves in 2D phononic crystals based on Dirichlet-to-Neumann map. Acta Mechanica Sinica 2012;28(4): 1143-1153.

[16] Li FL, Wang YS, Zhang CZ, Yu GL. Bandgap calculations of two-dimensional solid-fluid phononic crystals with the boundary element method. Wave Motion 2013;50(3): 525-541.

[17] Li FL, Wang YS, Zhang C. Boundary element method for bandgap computation of photonic crystals. Optics Communications 2012;285(5): 527-532.

[18] Li FL, Wang YS, Zhang C, Yu GL. Boundary element method for band gap calculations of two-dimensional solid phononic crystals. Engineering Analysis with Boundary Elements 2013;37(2): 225-235.
[19] Gao H, Xiang J, Zheng C, Jiang Y, Matsumoto T. BEM-based analysis of elastic banded material by using a contour integral method. Engineering Analysis with Boundary Elements 2015;53: 56-64.
[20] Zheng CJ, Chen HB, Gao HF, Du L. Is the Burton-Miller formulation really free of fictitious eigenfrequencies?. Engineering Analysis with Boundary Elements 2015; 59:43-51.
[21] Shi ZJ, Wang YS, Zhang CZ. Band structure calculation of scalar waves in two-dimensional phononic crystals based on generalized multipole technique. Applied Mathematics and Mechanics 2013; 34(9): 1123-1144.
[22] Shi ZJ, Wang YS, Zhang CZ. Application of the generalized multipole technique in band structure calculation of two-dimensional solid/fluid phononic crystals. Mathematical Methods in the Applied Sciences 2015;38(15): 3246-63.
[23] Shi ZJ, Wang YS, Zhang CZ. Band structure calculations of in-plane waves in two-dimensional phononic crystals based on generalized multipole technique. Applied Mathematics and Mechanics 2015;36(5): 557-80.
[24] Wang G, Wen JH, Han XY, Zhao HG. Finite difference time domain method for the study of band gap in two-dimensional phononic crystals. Acta Physica Sinica 2003;52(8): 1943-47.
[25] Sun JH, Wu TT. Propagation of acoustic waves in phononic-crystal plates and waveguides using a finite-difference time-domain method. Physical Review B 2007;76(10): 104304(1)-104304 (8).
[26] Yan Lu, Yang Yang, James K. Guest and Ankit Srivastava. 3-D phononic crystals with ultra-wide band gaps. Scientific Reports 2017; 7: 43407.
[27] Kuang W, Hou Z, Li Y and Li H. The band gaps of cubic phononic crystals with different shapes of scatterers. Journal of Physics D: Applied. Physics. 2006 ; 39: 2067–71
[28] Kansa EJ. Multiquadrics - A scattered data approximation scheme with applications to computational fluid dynamics. 1. Computers & Mathematics with Applications 1990;19(8-9): 127-45.
[29] Fasshauer GE. Meshfree Approximations with MATLAB. World Scientific Publishers, Singapore. 2007.
[30] Lin. J, Zhang C, Sun L, Lu J., Simulation of seismic wave scattering by embedded cavities in an elastic half-plane using the novel singular boundary method, Advances in Applied Mathematics and Mechanics 2018; 10 (2): 322-342.
[31] Wright G. and Fornberg B. Scattered node compact finite difference–type formulas generated from radial basis functions. Journal of Computational. Physics 2016; 212: 99–123.
[32] Wang LH, Radial basis functions methods for boundary value problems: Performance comparison. Engineering Analysis with Boundary Elements 2017; 84: 191-205.
[33] Martin B, Fornberg B, St-Cyr A. Seismic modeling with radial basis function generated finite differences. Geophysics 2015; 80(4): T137-T146.
[34] Sarler B, Vertnik R. Meshfree explicit local radial basis function collocation method for diffusion problems. Computers & Mathematics with Applications 2006;51(8): 1269-1282.

[35] Vertnik R, Sarler B. Meshless local radial basis function collocation method for convective-diffusive solid-liquid phase change problems. International Journal of Numerical Methods for Heat & Fluid Flow 2006; 16(5): 617-640.
[36] Liu X., Liu G., Tai K., and Lam K. Radial point interpolation method (RPICM) for partial differential equations. Computers & Mathematics with Applications 2005; 50:1425–1442.
[37]Bayona, V., Flyer N., Fornberg B. and Barnett G.A., On the role of polynomials in RBF-FD approximations: II. Numerical solution of elliptic PDEs, Journal of Computational Physics 2017; 332: 257-273.
[38] Martin B. and Fornberg B., Seismic modeling with radial basis function-generated finite differences (RBF-FD) – a simplified treatment of interfaces, Journal of Computational. Physics 2017; 335: 828-845.
[39] Hart EE, Cox SJ, Djidjeli K. Compact RBF meshless methods for photonic crystal modelling. Journal of Computational Physics 2011;230(12): 4910-4921.
[40] Zheng H, Zhang Ch, Wang YS, Sladek J, Sladek V. A meshfree local RBF collocation method for anti-plane transverse elastic wave propagation analysis in 2D phononic crystals. Journal of Computational Physics 2016;305: 997-1014.
[41] Zheng H, Zhang Ch, Wang YS, Sladek J, Sladek V. Band structure computation of in-plane elastic waves in 2D phononic crystals by a meshfree local RBF collocation method. Engineering Analysis with Boundary Elements 2016; 66: 77-90.
[42] Zheng H, Zhang Ch, Wang YS, Chen W, Sladek J, Sladek V. A local RBF collocation method for band structure computations of 2D solid/fluid and fluid/solid phononic crystals. International Journal for Numerical Methods in Engineering 2017; 110: 467-500.
[43] Zheng H, Yang Z, Zhang Ch, Tyrer M. A local radial basis function collocation method for band structure computations of phononic crystals with scatterers of an arbitrary geometry, Applied mathematical modeling 2018; 60: 447-459.
[44] C. Guillén-Gallegosa, H. Alva-Medranoa, H. Pérez-Aguilara, A. Mendoza-Suáreza, F. Villa-Villab. Phononic band structure of an acoustic waveguide that behaves as a phononic crystal, Results in Physics. 2019; 12: 1111-1118.